

Integrated Sensing and Communication System Based on Radio Frequency Resonance Beam

Yixuan Guo, Shuaifan Xia, Mingliang Xiong, *Member, IEEE*, Qingwen Liu, *Senior Member, IEEE*, Wen Fang, *Member, IEEE*, Qingwei Jiang, Gang Yan, *Member, IEEE* and Jiangchuan Mu

Abstract—To address the complex beam control in traditional multiple-input multiple-output (MIMO) systems, researchers have proposed adaptive beam alignment using retro-directive antenna (RDA) arrays. This approach creates echo resonance between the base station (BS) and user equipment (UE), significantly reducing computational load. However, conventional resonant beam systems (RBS) suffer from echo interference due to the shared uplink and downlink frequency. Therefore, this paper proposes an innovative resonance beam-based integrated sensing and communication (RB-ISAC) system designed for efficient passive sensing and bidirectional communication. In this system, the UE operates passively, with both the BS and UE utilizing a phase conjugation and frequency conversion structure to decouple uplink and downlink carrier frequencies, ensuring continuous electromagnetic wave oscillation between the two ends. Effective compensation for signal propagation loss enables resonance after multiple oscillations. At this point, the beam's field forms a low-diffraction-loss, highly focused pattern, automatically aligning the transmitter and receiver. This enables high-precision passive positioning alongside robust uplink and downlink communication. Simulation results demonstrate the proposed system achieves resonance within multiple iterations, supporting uplink and downlink communication up to 5 m, and enabling passive direction of arrival (DOA) estimation with an error under 2° .

Index Terms—Passive ISAC, resonant beam system, retro-directive antenna, MIMO, beamforming, direction of arrival, frequency division system.

I. INTRODUCTION

THE rapid development of wireless communication and intelligent technologies is driving increasing demands for emerging applications like the internet of things (IoT), vehicle-to-everything (V2X), and drone swarms. These applications require not only high communication throughput but also precise localization for normal equipment operation [1]. Consequently, single-function systems are no longer sufficient to meet these dual demands for high-precision localization and efficient communication [2], [3], and integrated sensing and communication (ISAC) systems have thus emerged as an essential component of future wireless networks [4], [5]. Effectively integrating localization and communication functions for resource sharing and collaborative optimization

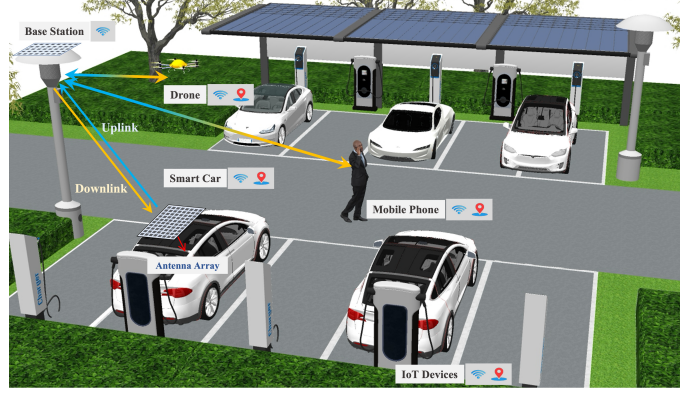


Fig. 1. Simultaneous localization and communication systems are used in smart parking lots, with downlink communication and uplink for localization.

holds significant practical importance and broad application prospects. Fig. 1 illustrates a typical application scenario, such as a smart parking lot, where the base station (BS) simultaneously provides communication services and obtains location information for IoT devices within the area, even for passive devices incapable of active signal transmission.

Millimeter-wave (mmWave) networks have gained significant attention in recent years as a wireless technology capable of supporting dynamic scenarios and diverse applications [6]. Due to mmWave's significantly higher propagation loss compared to lower frequency bands, beamforming (BF) techniques are essential to focus signal power, thereby extending propagation paths and enhancing communication performance. Researchers have explored optimizing mmWave BF matrices through learning-based methods to enhance network quality [7]. However, in large-scale multiple-input multiple-output (MIMO) systems, training overhead from a large number of antenna elements poses a major challenge. To address this, researchers have investigated installing sensors in the infrastructure to support mmWave communication, further reducing training complexity [8]. Beyond the communication domain, mmWave technology has also shown great potential in localization systems. Leveraging its ultra-wideband characteristics and large-scale antenna arrays, mmWave enables high-precision and robust localization. This is primarily due to the inverse relationship between antenna size and beam-width, which allows for highly focused beams [9], [10], [11], [12].

However, most current studies still focus on either communication or localization tasks individually, rather than addressing the ISAC scenarios. For applications requiring both high-

Y. Guo and J. Mu is with the Shanghai Research Institute for Intelligent Autonomous Systems, Tongji University, Shanghai 201210, China (e-mail: {guoyixuan, jiangchuan_mu}@tongji.edu.cn).

S. Xia, M. Xiong, Q. Jiang and Q. Liu is with the School of Computer Science and Technology, Tongji University, Shanghai 201804, China (e-mail: {collinxia, mlx, jiangqw, qliu}@tongji.edu.cn).

W. Fang is with the College of Electronics and Information Engineering, Tongji University, Shanghai 201804, China (e-mail: wen.fang@tongji.edu.cn).

G. Yan is with the School of Physics Science and Engineering, Tongji University, Shanghai 200092, China (e-mail: gyan@tongji.edu.cn).

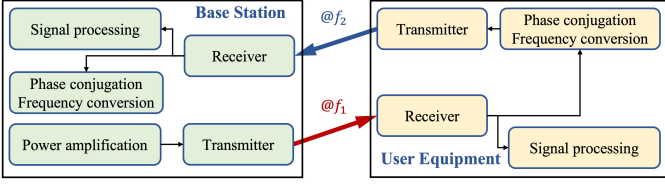


Fig. 2. Workflow of the resonant beam-based integrated localization and communication system.

efficiency communication and high-precision localization, there is an urgent need for a unified and efficient framework. The authors of [13], [14] investigated the joint transceiver design for ISAC systems. The authors of [15] explored the applications of ISAC in intelligent transportation, and the authors of [16] examined the communication resource allocation problem in drones-assisted ISAC scenarios.

It is evident that designing ISAC systems in the mmWave band faces multiple challenges. Firstly, under limited wireless resources, the core issue is how to simultaneously achieve high localization accuracy and high communication rates. Secondly, the complexity of beamforming also places higher demands on system design. In traditional communication systems, beamforming is primarily used to direct signal power to the receiver to optimize communication efficiency [17]. However, in ISAC systems, beamforming not only serves the communication function but also directly affects localization accuracy [18]. Therefore, reducing the complexity of beamforming control is critical, especially in large-scale MIMO systems.

In the optical frequency band, numerous studies have demonstrated that resonant beam systems (RBS) possess adaptive beam alignment characteristics. By installing two optical retro-reflective devices at the transmitting and receiving ends and allowing the laser to oscillate back and forth multiple times, waves of the same frequency and phase can superimpose, while waves with different phases gradually attenuate until they cancel out. This enables strongly directional BF without the need for channel estimation and beam control [19], [20], [21], [22]. Furthermore, existing research has confirmed that migrating RBS to the mmWave band can continue to retain these advantages, achieving high-precision passive localization [23], [24] and highly efficient wireless power transfer [25]. However, the RBS structure based on single-frequency round-trip propagation will generate echo interference when supporting communication. Since the uplink and downlink signals are transmitted on the same frequency, the reflected and retransmitted signals inevitably interfere with each other. This interference becomes particularly severe after multiple round trips, significantly degrading the demodulation quality of communication signals.

Building on existing research, we propose a novel resonant beam-based integrate sensing and communication (RB-ISAC) system that integrates mmWave localization technology into a frequency-division resonant beam system. As illustrated in Fig. 2, the BS initially radiates omnidirectional electromagnetic waves. Upon reaching the UE, a portion of these waves undergoes frequency conversion and phase conjugation before being retransmitted to the BS. The BS then repeats this process,

generating redirected waves towards the UE, with its power amplifier compensating for electromagnetic wave attenuation to ultimately establish both uplink and downlink channels autonomously.

The proposed system effectively resolves uplink/downlink interference while fully leveraging the high-resolution characteristics of the mmWave band. Crucially, the system adaptively achieves simultaneous localization and communication without requiring active signal transmission from the UE, offering a simpler solution for passive ISAC applications in the mmWave band.

- To address the beamforming complexity in existing mmWave ISAC systems, we propose an RB-ISAC system. Frequency division between uplink and downlink is realized using the phase-locked loops (PLL). Without the need for additional complex algorithmic controls, the system achieves adaptive formation of uplink and downlink links through signal recovery and enhancement mechanisms as well as frequency adjustment, significantly reducing implementation complexity.
- To solve the interference problem between uplink and downlink signals in traditional single-frequency round-trip RBS systems, we design a frequency-division passive localization scheme. This scheme overcomes the inability of radio frequency-based resonate beam passive localization systems to support communication. By separating the frequencies of uplink and downlink signals, it ensures power transmission efficiency while achieving high-quality signal transmission and high-precision passive localization.
- To validate the feasibility of the proposed system, an RB-ISAC analytical model is constructed. This model theoretically analyzes the conditions for achieving resonance and quantitatively evaluates communication quality and localization performance. Simulation results demonstrate that the proposed system exhibits excellent performance in both passive communication quality and localization accuracy, providing critical design guidance for practical deployment.

The remainder of this paper is organized as follows. Section II introduces the system structure design of the RB-ISAC and the principle of resonance formation. Section III provides a detailed mathematical analysis model, including the power circulation model of the RB-ISAC system, the communication channel model, and the direction of arrival (DOA) estimation method. Section IV presents the simulation results and their analysis, covering the resonance formation process, convergence analysis, communication quality evaluation, and DOA accuracy assessment. Finally, Section V summarizes the research findings of this paper.

II. SYSTEM DESIGN

In this section, we first present the system structure design of the PLL-based retro-directive antenna (RDA) array to achieve frequency separation for the uplink and downlink, ensuring that the initial phase of the output signal matches the phase of the received signal. Subsequently, by adjusting the spacing between array elements, we ensure that the output signal can

accurately point toward the signal source. Additionally, we explain the principle of achieving resonance in the RB-ISAC system.

A. The Principle of Frequency Division in RB-ISAC

The RB-ISAC system comprises a BS and a UE, where the BS and UE transmit/receive signals via planar arrays consisting of M and N RDAs, respectively. Figure. 3 depicts the system structure. We assume that the UE is semi-passive [26], meaning that although it is equipped with an RDA array, the UE does not need to actively transmit signals. Instead, the BS first spatially broadcasts an electromagnetic wave at frequency f_1 ; upon receiving this signal, the UE reflects it back to the BS at frequency f_2 using its RDA array. The BS captures the RF signal, which is then down-converted by an intermediate frequency (IF) mixer using a local oscillator (LO) signal $f_{LO,b}$. The mixer output passes through a band-pass filter (BPF) to retain the intermediate frequency component $f_{IF1,b} = f_2 - f_{LO,b}$.

Subsequently, the signal is directed through a splitter, with one portion of the IF signal routed to a base band (BB) mixer. The signal continues to be down-converted into a BB signal and fed into the signal processing unit (SPU) for further processing and analysis. The remaining signal enters frequency divider (FD) 1 in the phase-locked loop (PLL) for D_1 -fold frequency division. It is then compared with a reference signal that has undergone D_2 -fold frequency division in the phase detector, generating a phase error signal. This error signal is a voltage signal proportional to the phase difference. A loop filter is used to remove high-frequency noise and unwanted fluctuations, resulting in a smooth DC control voltage that adjusts the frequency of the voltage-controlled oscillator (VCO) [27].

At this point, the VCO generates an IF signal locked to the phase of its input signal, with a frequency of $f_1 - f_{LO}$. This signal undergoes up-conversion, where it is mixed with the IF signal f_{IF1} input to the PLL. This generates a new IF signal with a frequency of

$$f_{IF2,b} = f_1 + f_2 - 2f_{LO,b}. \quad (1)$$

The IF signal re-enters the PLL for frequency/phase locking until both phase and frequency errors reach zero [28], [29]. The locked signal then upconverts to RF frequency f_1 through mixing with the modulated signal, followed by power amplification for output. At this point, the relationship between the frequencies and phases of the PLL's input and output signals can be expressed as

$$\frac{f_{ref}}{D_2} = \frac{f_1 + f_2 - 2f_{LO,b}}{D_1}, \quad (2)$$

$$\frac{\varphi_{ref}}{D_2} = \frac{\varphi_1 + \varphi_2 - 2\varphi_{LO,b} + 2n\pi}{D_1}, \quad (3)$$

where f_{ref} and φ_{ref} are the frequency and phase of the reference signal, respectively. Assuming that both the LO signal and the reference signal have a phase of 0° , we can derive

$$f_1 = \frac{D_1}{D_2} f_{ref} + 2f_{LO,b} - f_2, \quad (4)$$

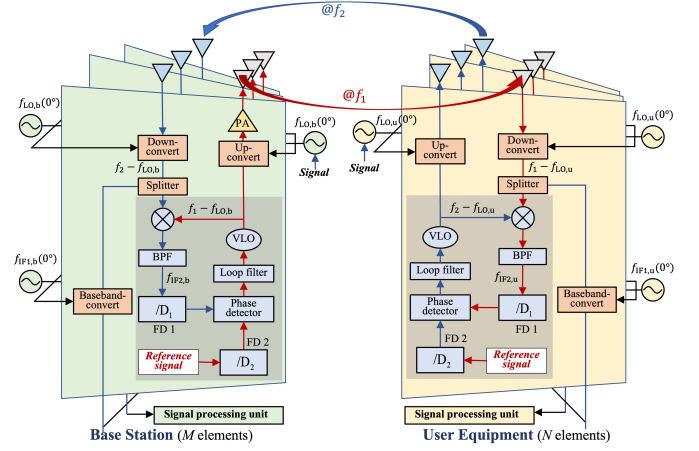


Fig. 3. Diagram of uplink and downlink frequency separation structure and conjugate circuit structure in resonant beam-based integrated localization and communication system.

$$\varphi_1 = -\varphi_2. \quad (5)$$

This demonstrates successful frequency conversion and phase conjugation through system processing, mitigating echo interference from identical uplink/downlink frequencies while ensuring signal return path conditions [30].

Here's a frequency setting example. Assume the downlink carrier frequency is $f_1 = 29$ GHz and the uplink carrier frequency is $f_2 = 31$ GHz. In this scenario, the VCO generates a 1 GHz signal, while the LO produces a $f_{LO,b} = 28$ GHz signal. Through frequency mixing, the first IF signal $f_{IF1,b} = 3$ GHz (obtained by mixing f_2 with the LO signal), and the second IF signal is $f_{IF2,b} = 1$ GHz (according to eq. 1). When the reference signal frequency $f_{ref} = 1$ GHz, frequency divisions can be set to $D_1 = 4$ and $D_2 = 1$.

The operation of the UE's antenna is similar to that of the BS. However, the BS must be equipped with a power amplifier to boost the output signal power, compensating for signal losses during transmission and ensuring that the downlink signal is strong enough to reach the UE. Additionally, the BS's signal processing unit needs to analyze the phase of the received signal to obtain the DOA information of the UE, while the UE does not require this capability.

B. Dual Frequency Resonance Principle

As mentioned above, both the BS and UE can recover the phase of the transmitted signal through the RDA arrays. However, due to the change in frequency, if only the initial phase is controlled, the transmitted signal and the received signal will inevitably not be parallel. Therefore, to ensure the backtracking of the signal, improvements to the array are necessary. As shown in Fig. 4, the phase difference between the i -th element and j -th element in the BS's Rx array can be expressed as

$$\Delta\varphi_{ij,b}^r = \frac{2\pi}{\lambda_2} d_{ij,b}^r, \quad (6)$$

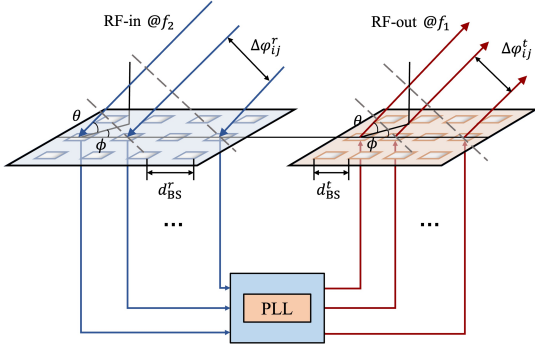


Fig. 4. Schematic diagram of the principle of RB-ISAC echo signal original path return.

where λ_2 is the wavelength of the carrier signal with frequency f_2 , and $d_{ij,b}^r$ denotes the distance between the i -th and j -th element of the Rx array. It can be represented by DOA as

$$d_{ij,b}^r = d_{BS}^r (i \sin \theta \cos \phi + j \sin \theta \sin \phi), \quad (7)$$

where d_{BS}^r is the Rx element spacing of the BS, θ is the elevation angle, and ϕ is the azimuth angle. To ensure the received and transmitted waves are parallel, the azimuth and elevation angles of the received wave must match those of the transmitted wave, and their phase differences should satisfy $\Delta \varphi_{ij}^t = \Delta \varphi_{ij}^r$. We can obtain:

$$\frac{2\pi d_{ij,b}^r}{\lambda_2} = \frac{2\pi d_{ij,b}^t}{\lambda_1}, \quad (8)$$

where $d_{ij,b}^t$ is the elements spacing of the Tx array, and λ_1 is the transmitted signals wavelength. Therefore, the spacing between the elements of the Tx array and the Rx array should satisfy

$$\frac{d_{ij}^r}{d_{ij}^t} = \frac{f_1}{f_2}. \quad (9)$$

The phase-conjugated signal with frequency f_2 can be generated and redirected to the UE [31], [32]. The RDA array on the UE side follows a similar process.

The BS and UE ensure the parallelism of the downlink and uplink by processing the phase of the received signal through conjugation and frequency separation. Specifically, the BS utilizes the conjugate phase information of the received signal to adjust the direction of the transmitted beam, precisely pointing it toward the location of the UE. On the UE side, the RDAs processes the received signal in the same manner through conjugation and frequency division, and then reflects the signal back to the BS. Through this iterative back-and-forth process, electromagnetic waves in space form a standing wave pattern along a specific path, achieving beam self-alignment between the BS and UE.

III. ANALYTICAL MODEL

In this section, we first establish a downlink and uplink signal transmission circulation model for the RB-ISAC system and analyze the conditions for the system to reach a steady state. Then, the channel model of the proposed system is presented, including the expressions for downlink and uplink signals.

Finally, we estimate the DOA of the BS received signal using the MUSIC algorithm.

A. Power Circulation Model

In the RB-ISAC system, signal transmission and efficiency are crucial for signal enhancement and closed-loop signal transmission in the uplink and downlink. Specifically, the UE does not need to actively transmit signals. The BS initially radiates electromagnetic waves with a central frequency of f_1 into space. Upon receiving the signal from the BS, the RDA array of the UE uses a LO and a mixer to return the electromagnetic waves to the BS at a central frequency of f_2 . The power density of the uplink signal received by the m -th antenna on the BS plane can be expressed as

$$W_{BS,m}^r = \sum_{n=1}^N \frac{1}{4\pi} P_{UE,n}^t G_{UE,n} l_{nm}^{-\alpha}, \quad (10)$$

where $P_{UE,n}^t$ and $G_{UE,n}$ represent the transmitted power and antenna gain of the n -th antenna of the UE, respectively. l_{nm} is the distance between the m -th antenna on the BS and the n -th antenna on the UE, and α is the path loss exponent.

According to electromagnetic wave theory [33], the time-averaged power density per unit area can be represented using the Poynting vector

$$W = \frac{1}{2} \vec{E} \cdot \vec{H}, \quad (11)$$

where \vec{E} and \vec{H} are the electric field intensity and magnetic field intensity, respectively. In free space or a uniform medium, the relationship between the electric field and the magnetic field is $\vec{H} = \vec{E}/\eta$, where η is the characteristic impedance (wave impedance) of the medium. Therefore

$$W = \frac{|\vec{E}|^2}{2\eta}. \quad (12)$$

Thus, the electric field intensity of the electromagnetic wave radiated from the UE to the BS can be expressed as

$$E_{BS,m}^r = \sum_{n=1}^N \sqrt{\frac{\eta}{2\pi} P_{UE,n}^t G_{UE,n} l_{nm}^{-\alpha}} e^{j(\Delta \varphi_{nm} + \varphi_{err})}, \quad (13)$$

where $\Delta \varphi_{nm} = k_2 l_{nm}$ represents the phase difference of the signal transmitted from the n -th antenna of the UE to the m -th antenna of the BS, $k_2 = 2\pi/\lambda_2$ is the wavenumber of the uplink electromagnetic wave, and λ_2 is the wavelength corresponding to the central frequency f_2 , φ_{err} is the phase noise of the PLL.

The signal power received by the BS is determined by the effective reception area of the antenna and the signal intensity on the BS surface

$$\begin{aligned} P_{BS}^r &= \sum_{m=1}^M \frac{G_{BS,m} \lambda_2^2}{8\pi\eta} (E_{BS,m}^r)^2 \\ &= \frac{\lambda_2^2}{16\pi^2} \sum_{m=1}^M \sum_{n=1}^N \left| \sqrt{P_{UE,n}^t G_{UE,n} G_{BS,m} l_{nm}^{-\alpha}} e^{j(\Delta \varphi_{nm} + \varphi_{err})} \right|^2, \end{aligned} \quad (14)$$

where $G_{BS,m}$ is the gain of the m -th antenna on the BS.

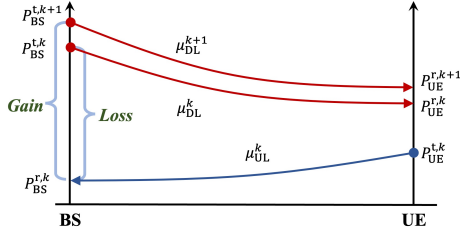


Fig. 5. Gain and loss of the system during oscillation process.

After receiving the signal from the UE, the BS extracts the necessary signals for localization and communication through a signal processing module. The remaining signal power is amplified to a predetermined gain to compensate for the unavoidable power loss during propagation. The signal frequency is then converted to f_1 , and the signal undergoes phase conjugation through the RDAs before being retransmitted to the UE, achieving bidirectional transmission. The actual transmitted signal power from the BS can be expressed as

$$P_{BS}^t = G_{PA}(1 - \beta_{com} - \beta_{loc})P_{BS}^r, \quad (15)$$

where G_{PA} is the power gain of the BS power amplifier, β_{com} represents the proportion of the received signal power at the BS used for communication, β_{loc} represents the proportion used for localization. After retransmission, the downlink signal power received by the UE is

$$P_{UE}^r = \frac{\lambda_2^2}{16\pi^2} \sum_{m=1}^M \sum_{n=1}^N \left| \sqrt{P_{BS,m}^t G_{UE,n} G_{BS,m} l_{mn}^{-\alpha}} e^{j(\Delta\varphi_{mn} + \varphi_{err})} \right|^2 \quad (16)$$

It should be noted that even if the uplink and downlink link lengths are the same, the phase differences may not necessarily match due to the difference in carrier frequencies.

When the UE receives the electromagnetic waves from the BS, not all the received power is directly utilized for uplink signal transmission. A portion of the power is allocated to the signal processing module to extract the communication-required information, as well as to support the basic operation of the equipment, such as frequency conversion and signal processing functions. The remaining power is adjusted to the uplink frequency and then returned to the BS via phase-conjugated operations, expressed as

$$P_{UE}^t = (1 - \gamma_{com} - \gamma_{wok}) P_{UE}^r, \quad (17)$$

where γ_{com} denotes the proportion of the received signal power used for communication, and γ_{wok} denotes the proportion allocated to support the basic operation.

The downlink and uplink transmission efficiency at can be defined as

$$\begin{cases} \mu_{DL} = P_{UE}^r / P_{BS}^t \\ \mu_{UL} = P_{BS}^r / P_{UE}^t \end{cases} \quad (18)$$

Note that the received and transmitted power mentioned here are both in the same oscillation round.

As shown as Fig. 5, during the k -th oscillation, the power loss of the RB-ISAC system can be represented as

$$\begin{aligned} P_{BS}^{t,k} - P_{BS}^{r,k} &= P_{BS}^{t,k} - (1 - \gamma_{com} - \gamma_{wok}) \mu_{UL} P_{UE}^{r,k} \\ &= P_{BS}^{t,k} - (1 - \gamma_{com} - \gamma_{wok}) \mu_{UL}^k \mu_{DL}^k P_{BS}^{t,k}, \end{aligned} \quad (19)$$

where $P_{BS}^{t,k}$ and $P_{BS}^{r,k}$ represent the transmitted and received signal powers of the BS during the k -th oscillation, respectively, and $P_{UE}^{r,k}$ represents the signal power transmitted by the UE during the k -th oscillation.

Similarly, at the beginning of the $(k+1)$ -th oscillation, the power gain of the BS's amplifiers for each antenna can be expressed as

$$P_{BS}^{t,k+1} - P_{BS}^{r,k} = P_{BS}^{t,k+1} - (1 - \gamma_{com} - \gamma_{wok}) \mu_{UL}^k \mu_{DL}^k P_{BS}^{t,k}. \quad (20)$$

From (19) and (20), it can be observed that when k is relatively small, the gain must exceed the loss to ensure the quality of signals in the uplink and downlink transmission process. When the number of oscillation reaches a large value, (19) and (20) become equal, RB-ISAC achieves a steady state. At this point, the amplifier compensates for the propagation loss of electromagnetic waves in a single oscillation, and the system reaches its optimal state. The power efficiency also achieves its peak, and the power transmitted and received by the BS converges to a constant value. The electric field distribution becomes stable, which is beneficial for passive localization as the received signal strength remains stable and directionality is evident.

B. Channel Model

In wireless communication systems, accurate channel modeling is a crucial step in analyzing and optimizing system performance. In the RB-ISAC system, the BS and UE generate communication carriers embedded with information through modulators and radiate them via RDA arrays. The downlink carrier signal radiated by the m -th BS can be expressed as

$$S_{BS,m}^t = \sqrt{2\eta P_{BS,m}^t} e^{j(2\pi f_2 t + \varphi_m)}. \quad (21)$$

The downlink carrier signal is emitted by the BS antenna array, where each antenna element independently radiates into space with a unique phase φ_m and covers the entire space. The received effective carrier signal matrix by the UE from the BS can be expressed as

$$\mathbf{S}_{UE}^r = \mathbf{H}_{DL} \mathbf{S}_{BS}^t + \mathbf{n}, \mathbf{S}_{UE}^r \in \mathbb{C}^{N \times 1}, \quad (22)$$

where $\mathbf{S}_{BS}^t = \{S_{BS,1}^t, \dots, S_{BS,M}^t\} \in \mathbb{C}^{M \times 1}$ is the transmission matrix of the BS, and $\mathbf{n} \in \mathbb{C}^{N \times 1}$ is the additive white Gaussian noise (AWGN) which variance $\sigma_{DL}^2 = 2\eta\kappa T B_{DL}$ and it is uniformly distributed and independently and identically distributed (i.i.d.), κ is the Boltzmann constant, and $\kappa = 1.38 \times 10^{-23}$ J/K, T is the ambient temperature, and B_{DL} is the downlink

carrier bandwidth [34]. $\mathbf{H}_{DL} = \begin{bmatrix} h_{DL}^{11} & \dots & h_{DL}^{1M} \\ \vdots & \ddots & \vdots \\ h_{DL}^{N1} & \dots & h_{DL}^{NM} \end{bmatrix} \in \mathbb{C}^{N \times M}$ is the channel gain matrix composed of channel gains between

different elements of UE and BS, and the downlink channel gain h_{DL}^{mn} can be expressed as

$$h_{\text{DL}}^{mn} = \frac{\lambda_2}{4\pi} \sqrt{G_{\text{UE},n} G_{\text{BS},m} l_{mn}^{-\alpha}} e^{j(\Delta\varphi_{mn} + \varphi_{\text{err}})}, \quad (23)$$

where λ_2 is the wavelength corresponding to the downlink carrier frequency, $G_{\text{UE},n}$ and $G_{\text{BS},m}$ are the gains of the UE and BS antennas, respectively, l_{mn} is the distance between the m -th BS antenna and the n -th UE antenna, and α is the path loss exponent [25], [35].

After receiving the signal from the BS, the UE generates a signal through PLL to recover the phase of the downlink signal for uplink transmission.

Then, the uplink base band signal of the n -th UE antenna is modulated onto the carrier signal, and its frequency is converted to f_1 via an RF mixer, generating the final uplink transmission carrier signal from the UE. This signal can be mathematically expressed as

$$s_{\text{UE},n}^t = \sqrt{2\eta P_{\text{UE},n}^t} e^{j(2\pi f_1 t + \varphi_n)}. \quad (24)$$

This marks the end of one iterative cycle. The signal-to-noise ratio (SNR) of the downlink signal received at the RDA of UE is defined as the ratio of the total received signal power used for communication to the noise power and can be expressed as

$$\text{SNR}_{\text{DL}} = \frac{\gamma_{\text{com}} P_{\text{UE}}^t}{2\eta \kappa T B_{\text{DL}}}. \quad (25)$$

Assuming both BS and UE have perfect channel state information (CSI), the maximum achievable total data rate for the downlink carrier can be expressed as

$$R_{\text{DL}} = B_{\text{DL}} \log_2(1 + \text{SNR}_{\text{DL}}). \quad (26)$$

On the other hand, spectral efficiency (SE) is another critical metric for evaluating the performance of a communication system. SE reflects the average number of bits transmitted per unit of bandwidth, providing a direct indication of the system's ability to transfer information within limited spectral resources. It is a key parameter in the design and optimization of communication systems and can be expressed as

$$\zeta_{\text{DL}} = \frac{R_{\text{DL}}}{B_{\text{DL}}} = \log_2 \left(1 + 10^{0.1(\text{SNR}_{\text{DL}} - \mathcal{L})} \right), \quad (27)$$

where the \mathcal{L} is the channel loss. Combining with (26), it is evident that higher power transfer efficiency contributes to maximizing the system's communication performance under limited bandwidth resources. It is noteworthy that quantization noise causes SNR saturation, thereby limiting the maximum value of spectral efficiency [36].

C. DOA Estimation

In the RB-ISAC system, DOA estimation is a critical step for achieving spatial localization and beamforming. By analyzing the signal distribution characteristics on the receiving antenna array, the location of the signal source relative to the array center can be inferred. This process typically involves the construction of the array signal model and the application of high-resolution DOA estimation algorithms. This section provides a detailed analysis of the processing of signals received

by the BS from the UE and discusses the principles of DOA estimation using the MUSIC algorithm. After receiving the reflected pass-band signal from the UE, the BS downconverts it to a base band signal by mixing it with the LO signal using the IF mixer. A portion of this signal is then directed to the SPU for DOA estimation. For analytical convenience, the SPU received base band signal matrix can be expressed as

$$\mathbf{S}_{\text{loc}} = \sqrt{\beta_{\text{loc}}} \mathbf{a}(\theta, \phi) \mathbf{S}_{\text{UE}}^t + \mathbf{n}, \quad (28)$$

where $\mathbf{S}_{\text{loc}} \in \mathbb{C}^{M \times 1}$ represents the SPU received signal vector of BS, encompassing signals from all array elements. The vector \mathbf{a} is the steering vector of the UE array center point, expressed as

$$\mathbf{a}(\theta, \phi) = \text{vec}(\mathbf{a}_x(\theta, \phi) \otimes \mathbf{a}_y(\theta, \phi)), \quad (29)$$

where the steering vectors in the x and y directions can be further represented as

$$\mathbf{a}_x(\theta, \phi) = [1 \exp\{jk d \sin \theta \cos \phi\} \dots \exp\{jk(\sqrt{M} - 1)d \sin \theta \cos \phi\}]^T, \quad (30)$$

$$\mathbf{a}_y(\theta, \phi) = [1 \exp\{jk d \sin \theta \sin \phi\} \dots \exp\{jk(\sqrt{M} - 1)d \sin \theta \sin \phi\}]^T. \quad (31)$$

By employing array signal processing techniques, such as the MUSIC algorithm, and utilizing the orthogonality between the signal vector and the noise vector, the position of the signal source relative to the receiving array center can be inferred. First, the covariance of the received signal at the BS can be calculated as

$$\begin{aligned} \mathbf{R}_r &= \mathbb{E}[\mathbf{S}_{\text{loc}} \mathbf{S}_{\text{loc}}^H] \\ &= \mathbf{a} \mathbb{E}[\mathbf{S}_{\text{UE}}^t \mathbf{S}_{\text{UE}}^{tH}] \mathbf{a}^H + \mathbb{E}[\mathbf{n} \mathbf{n}^H] \\ &= \mathbf{a} \mathbf{R}_s \mathbf{a}^H + \mathbf{R}_n. \end{aligned} \quad (32)$$

Assuming that the noise is a zero-mean complex Gaussian random variable, its covariance matrix can be expressed as $\mathbf{R}_n = \sigma_{\text{UL}}^2 \mathbf{I}$. Based on the covariance matrix \mathbf{R}_r , eigenvalue decomposition can be performed to obtain the signal subspace and the noise subspace

$$\mathbf{R}_r = \mathbf{U}_s \mathbf{\Lambda}_s \mathbf{U}_s^H + \mathbf{U}_n \mathbf{\Lambda}_n \mathbf{U}_n^H, \quad (33)$$

where $\mathbf{U}_s \in \mathbb{C}^{M \times 1}$ represents the signal subspace of the BS received signal, containing the eigenvectors corresponding to the signal, and $\mathbf{U}_n \in \mathbb{C}^{M \times (M-1)}$ represents the noise subspace, containing the $M - 1$ noise eigenvectors. $\mathbf{\Lambda}$ represents the diagonal matrix of eigenvalues.

The fundamental assumption of the MUSIC algorithm is that the steering vector corresponding to the signal direction is orthogonal to the noise subspace. For the true DOA, this relationship satisfies

$$\mathbf{a}^H \mathbf{U}_n = 0. \quad (34)$$

Based on this property, MUSIC constructs a spectral function

$$P_{\text{MUSIC}}(\theta, \phi) = \|\mathbf{U}_n^H \mathbf{a}(\theta, \phi)\|^{-2}, \quad (35)$$

where $\mathbf{U}_n^H \mathbf{a}(\theta, \phi)$ represents the projection of the steering vector onto the noise subspace. By searching for the peaks of the MUSIC spectrum, the DOA information of the UE can be estimated.

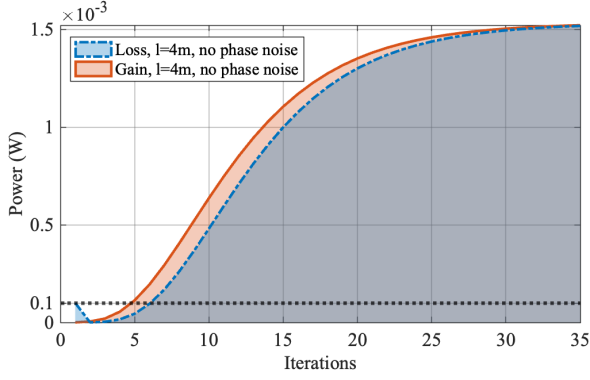


Fig. 6. The process of system loss and gain changing with iteration.

IV. PERFORMANCE EVALUATION

TABLE I
PARAMETER SETTING

Parameter	Symbol	Value
Carrier frequency of downlink and uplink	f_1, f_2	29, 31 GHz
Wavelength of downlink and uplink	λ_1, λ_2	(1.03, 0.97) cm
BS Tx and UE Rx antenna element spacing	d_{BS}^t, d_{UE}^r	0.48 cm
BS Rx and UE Tx antenna element spacing	d_{BS}^r, d_{UE}^t	0.52 cm
Power ratio of BS and UE communication	$\beta_{com}, \gamma_{com}$	0.1
Power ratio of BS used for localization	β_{loc}	0.1
Power ratio of UE used for operation	γ_{work}	0.2
Phase noise of PLL	φ_{err}	0.3 rad [37]
Antenna gain	$G(\theta, \phi)$	≤ 4.97 dBi [38]
RDA array size	M, N	40×40 [23]
Ambient temperature	T	295 K
Wave impedance	η	377Ω [33]
Path loss factor	ξ	3 dB [39]
Link length	l	{3, 4, 5} m
Path loss exponent	α	2
Initial input power of BS	$P_{BS}^{t,0}$	0.1 mW
Monte Carlo number	I	100

In this section, we conduct a simulation analysis of the system performance for the dual-frequency RB-ISAC. First, we illustrate the process by which the system achieves resonance through iterations. Then, we evaluate the communication metrics of the system, including transmission efficiency, SNR, and SE. Finally, we analyze the accuracy of the system's passive DOA estimation. Table I provides the parameters used in the simulation.

A. Establishment of Resonance

Figure 6 illustrates the system gain and loss variation with the number of iterations, omitting phase noise for clarity. Based on equations (19) and (20), the system reaches a steady state when the gain and loss per iteration effectively cancel each other out. Initially, as shown in Fig. 6, system loss exceeds gain. This is because the BS's initial 0.1 mW omnidirectional

radiation results in low power reception at the UE during the first iteration. However, as iterations progress, both system gain and loss increase. Before the 30-th iteration, gain consistently surpasses loss. Beyond 30 iterations, both metrics gradually stabilize and essentially balance, indicating the system has established resonance and achieved stable signal strength. This lays the foundation for subsequent communication and passive localization.

Fig. 7 illustrates the normalized distribution of spatial signal strength in the xoz -plane, comparing the downlink and uplink signal distributions during the initial transmission stage and after the system reaches a steady state.

As seen in Fig. 7(a), during the initial downlink transmission, the signal power emitted by the BS diffuses widely, primarily concentrating near the BS. An effective directional path hasn't yet formed, leading to significant signal loss in space and low power reaching the UE, resulting in poor transmission efficiency. Fig. 7(b) shows the uplink's spatial signal strength as the passive UE reflects a small portion of the received signal back along the original path via the RDAs. At this stage, the uplink transmission experiences severe scattering and lacks strong directionality. As iterations progress, the spatial electromagnetic field begins to self-replicate, ultimately forming resonance. Fig. 7(c) presents the downlink's spatial signal strength distribution once the system reaches a steady state. Clearly, the signal power forms a highly directional and focused transmission path in space, peaking along the direct line between the BS and the UE. Similarly, Fig. 7(d) displays the uplink's spatial signal strength after the system achieves resonance. Compared to Fig. 7(b), the signal strength distribution is significantly improved, with power highly focused along the direct line between the UE and the BS. This confirms that the system, through iterative optimization, gradually establishes a stable resonance path, enabling highly directional electromagnetic wave transmission. This outcome is crucial for realizing integrated passive communication and localization.

Fig. 8 illustrates how the number of iterations and link length affect the RB-ISAC system's transmission efficiency and SNR.

Fig. 8 (a) presents the transmission efficiency variation with iterations across different link lengths. As iterations increase, transmission efficiency steadily improves and eventually stabilizes. For shorter link length ($l = 3$ m), both the uplink and downlink transmission efficiencies converge to high levels near 0.8, demonstrating excellent transmission performance. However, for longer link lengths ($l = 4$ m and $l = 5$ m), the final converged transmission efficiencies are lower. In particular, at $l = 5$ m, the transmission efficiency less than 0.5. This highlights the significant impact of link length on transmission efficiency, where increased length leads to greater signal attenuation and noise, thus reducing overall efficiency.

In Fig. 8 (b), we further explore SNR variation with iterations under different link lengths. Simulation results indicate that SNR significantly increases during initial iterations before gradually converging. This improvement stems from the continuous increase in uplink and downlink transmission efficiency as iterations progress, leading to stronger received signal strengths at both the BS and UE. However, for long-

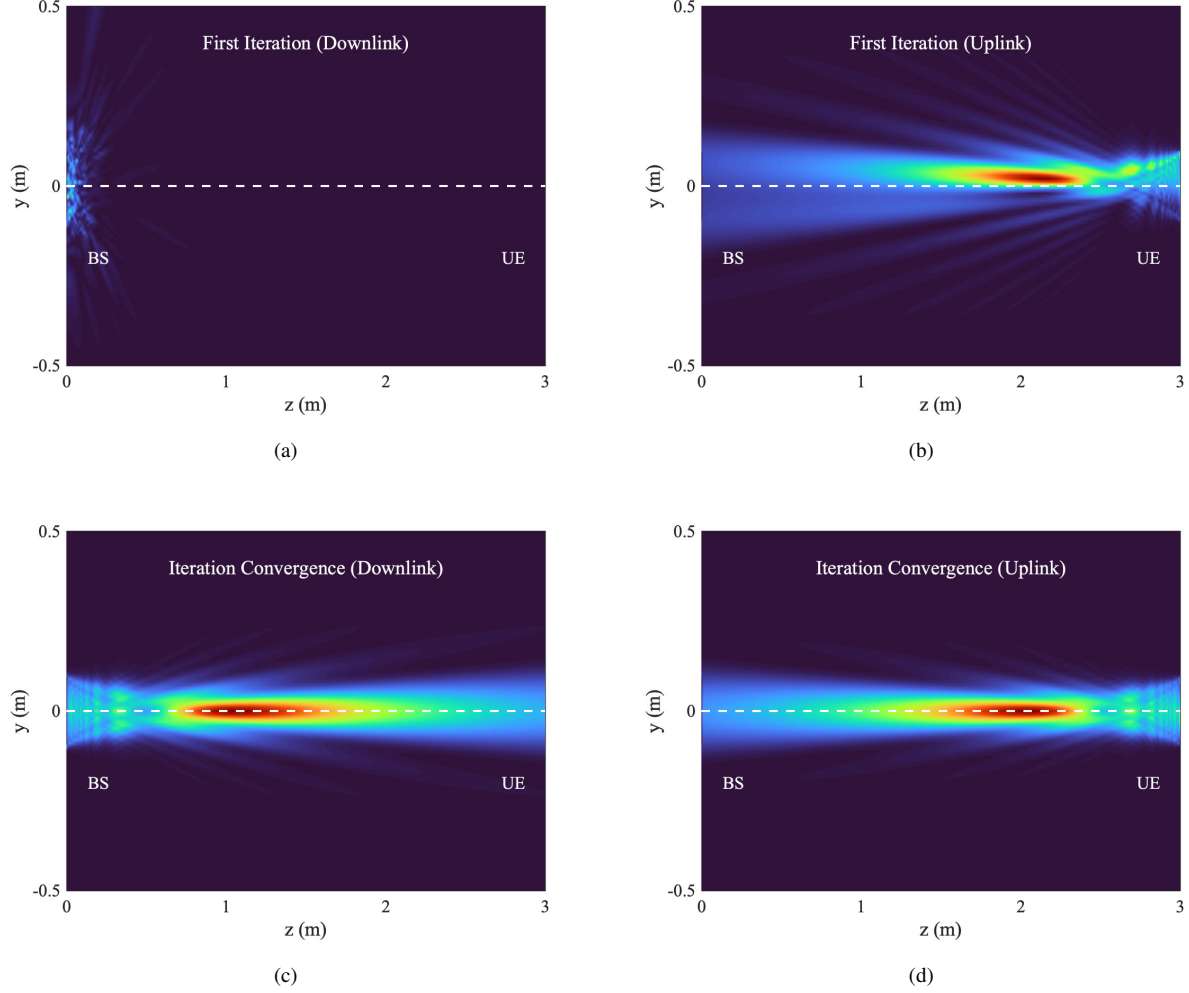


Fig. 7. Normalized distribution of spatial signal strength in xoz -plane. (a) Distribution of signal strength for the first transmission of the downlink; (b) The strength distribution of the first transmission signal on the uplink; (c) After the system reaches steady state, the distribution of downlink signal strength; (d) After the system reaches steady state, the distribution of uplink signal strength.

distance transmission, the signal strength naturally diminishes.

Fig. 9 depicts the relationship between SE and the number of iterations across different link lengths. The results show that for short link ($l = 3$ m), SE rapidly increases during early iterations. However, for $l = 4$ m and $l = 5$ m, the SE improvement rate is slower, with lower final converged values. Notably, at $l = 5$ m, the SE converges less than 1 bps/Hz. This decline is attributed to the reduction in SNR with increased link length, requiring more iterations to achieve optimal communication quality. This ensures that the RB-ISAC system can continuously provide higher-quality communication services to the UE. In summary, it can be seen that the communication quality of RB-ISAC can be rapidly improved during the process of establishing resonance. In the next section, we provide a detailed analysis of the communication performance of the RB-ISAC system under different DOA conditions.

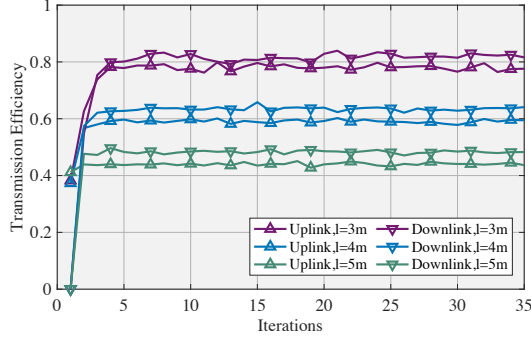
B. Communication Performance Analysis

In the RB-ISAC system, the elevation angle directly impacts antenna gain. Therefore, Fig. 10 illustrates the effects of

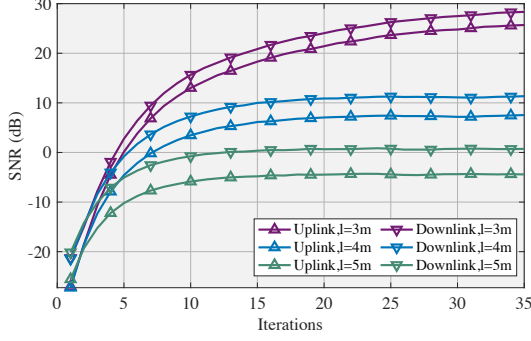
elevation angle and link length on the transmission efficiency and SNR of the system.

Fig. 10 (a) shows the variation in transmission efficiency with elevation angle under different link lengths. It can be observed that for shorter link length (e.g., $l = 3$ m), the system's transmission efficiency is highest, especially in lower elevation angle regions. This indicates that under short link lengths and ideal antenna alignment, the RB-ISAC system demonstrates exceptionally high robustness in communication. As the link length increases to $l = 4$ m and $l = 5$ m, the transmission efficiency decreases, and the influence of elevation angle becomes more pronounced.

In Fig. 10 (b), we further explore the relationship between SNR and elevation angle under different link lengths. Similarly, for short links ($l = 3$ m), the SNR remains high across the entire elevation angle range. This is because, in short-distance communication, signal attenuation is minimal, the signal power dominates, and the noise effect is negligible. However, for longer link lengths ($l = 4$ m and $l = 5$ m), SNR decreases significantly with increasing elevation angle, especially at high

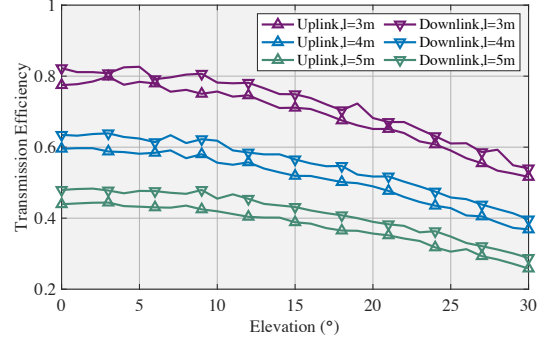


(a)

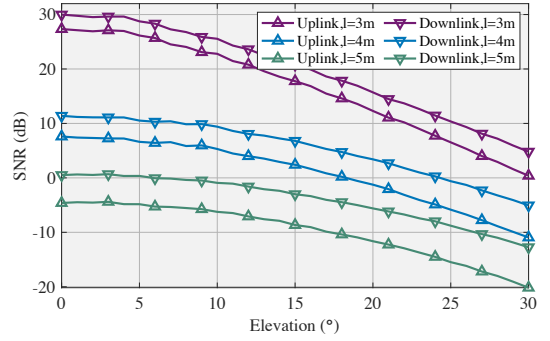


(b)

Fig. 8. System performance analysis with iteration times. (a) transmission efficiency analysis; (b) SNR analysis.



(a)



(b)

Fig. 10. System performance analysis with different elevation. (a) transmission efficiency analysis; (b) SNR analysis.

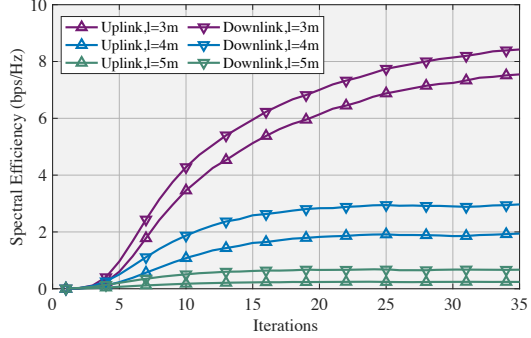


Fig. 9. Spectrum efficiency analysis with iteration times.

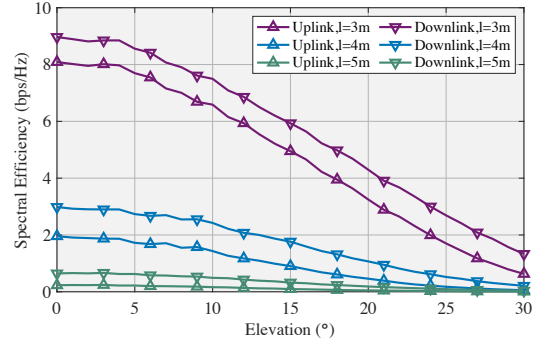


Fig. 11. Spectrum efficiency analysis with different elevation.

angles. Notably, the downlink SNR declines more slowly than the uplink due to the power amplifier's effect. This highlights the nonlinear relationship between SNR and spatial angles, underscoring the importance of beam alignment for high-quality communication.

Fig. 11 illustrates the SE variation with elevation angle under different link conditions. For short link ($l = 3$ m), SE is minimally affected by the elevation angle. However, as the link length increases, SE declines noticeably. At $l = 5$ m, this decline is more severe, exhibiting a sharp decay trend with increasing elevation angle. Specifically, at high angles (e.g., 30°), the SE of long links approaches zero. This is because increased link length leads to greater transmission losses, significantly reducing the system's channel capacity.

These simulation results reveal that link length and elevation

angle are critical factors influencing system communication performance. Under short link conditions, the RB-ISAC system exhibits high robustness. These findings suggest that in practical deployments, optimizing the geometric configuration of the links is essential. Particularly for long-distance and high-angle scenarios, RB-ISAC should incorporate beam self-alignment and effective signal gain compensation techniques to enhance overall system performance.

C. Passive DOA Estimation Analysis

In Fig. 12, we conduct a simulation analysis of the DOA estimation performance of RB-ISAC using the MUSIC algorithm at different link lengths. In Fig. 12 (a), the spectral peaks are prominent and concentrated, indicating that the algorithm achieves high resolution and accuracy under near-distance

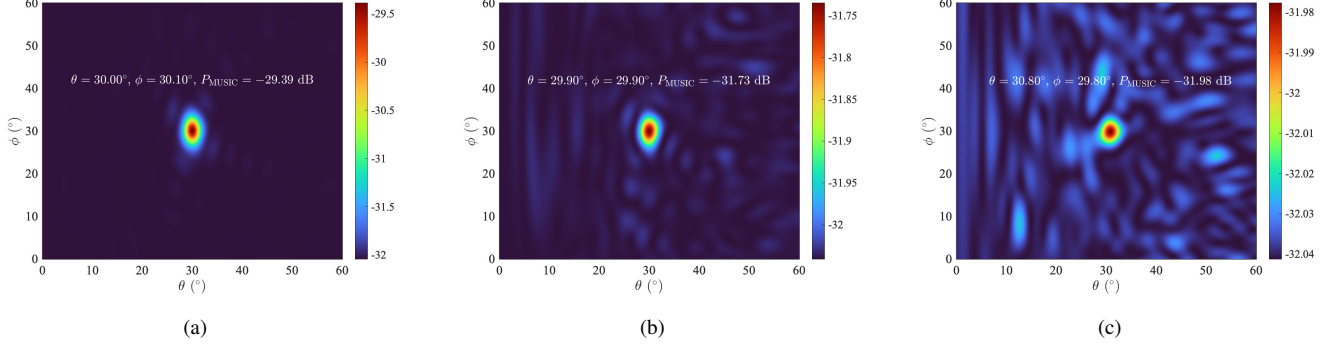


Fig. 12. The DOA estimation results of RB-ISAC system at different link lengths have true value of $\theta = \phi = 30^\circ$. (a) $l=3\text{m}$; (b) $l=4\text{m}$; (c) $l=5\text{m}$.

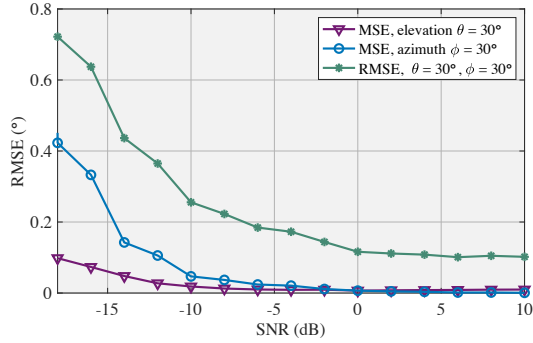


Fig. 13. The RMSE of RB-SLAC system in different SNR.

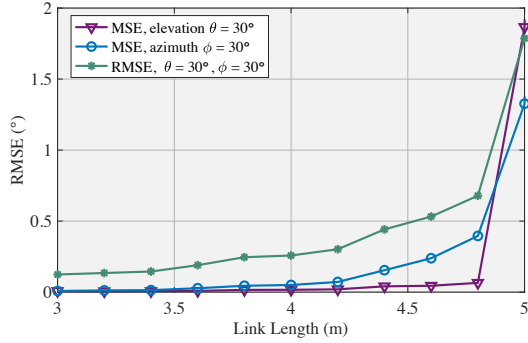


Fig. 14. The RMSE of RB-SLAC system in different link length.

conditions. This is attributed to the high SNR, which ensures stable estimation results without significant noise interference. As the link length increases to 4m (Fig. 12 (b)), the spectrum becomes less clear due to noise interference. The increased path loss from the greater link length leads to a reduction in SNR, and the spectral peak values also diminish. When the link length is further extended to 5m (Fig. 12 (c)), the received signal strength weakens further, and background noise intensifies. Consequently, the MUSIC algorithm's estimation accuracy and spectral peak resolution decline, resulting in the largest localization error.

In Fig. 13, we have demonstrated the distribution of root mean square error (RMSE) obtained through 100 Monte Carlo experiments. As a crucial metric for evaluating model prediction

accuracy, RMSE reflects the deviation between predicted and actual values. It is derived from the mean square error (MSE) of the elevation and azimuth angles [40], expressed as

$$\text{RMSE} = \sqrt{\text{MSE}_\theta + \text{MSE}_\phi}$$

$$= \sqrt{\frac{1}{I} \sum_{i=1}^I \{(\theta_i - \theta_0)^2 + (\phi_i - \phi_0)^2\}}, \quad (36)$$

where the θ_0 and ϕ_0 are the true values. From the figure, it is evident that as the SNR increases, the DOA estimation error decreases significantly due to the diminishing influence of noise. Notably, the RMSE of the elevation angle is consistently lower than that of the azimuth angle, indicating that the RB-ISAC system demonstrates higher sensitivity and accuracy in elevation angle estimation.

In Fig. 14, we show the RMSE performance of the RB-SLAC system at different link lengths. The elevation angle, azimuth angle, and overall RMSE were evaluated separately in the figure. From the Fig. 14, it can be seen that when the link length is between 3 m and 4.5 m, the RMSE remains relatively low and stable, indicating that the system can achieve high localization accuracy within this range. However, when the link length approached 5 m, the RMSE of all indicators shows a significant increase. This performance degradation is caused by signal attenuation, which has a negative impact on the accuracy of DOA estimation.

V. CONCLUSION

In this paper, we proposed a novel passive RB-ISAC system that utilized the self-alignment and power concentration characteristics of resonant beams for passive sensing and communication. By implementing signal recovery and enhancement mechanisms along with frequency adjustments, the system achieved closed-loop transmission of both uplink and downlink signals. Specifically, to address the interference caused by echoes in RF resonant localization systems, we have established a dual frequency resonant system using a PLL based RDA array in the mmWave band. Subsequently, we developed an electromagnetic wave circulation model for RB-ISAC, analyzed the conditions for resonance formation and channel characteristics, and performed DOA estimation

based on the signals reflected back from UE received by the BS. Finally, simulations validated that the proposed system could achieve resonance after multiple iterations through effective compensation for signal propagation loss, enabling high-precision passive DOA estimation while supporting uplink and downlink communication. This approach simplified the beam control complexity of traditional MIMO-ISAC systems and reduced the computational load of the system.

REFERENCES

- [1] F. Liu, Y. Cui, C. Masouros, J. Xu, T. X. Han, Y. C. Eldar, and S. Buzzi, "Integrated sensing and communications: Toward dual-functional wireless networks for 6G and beyond," *IEEE J. Sel. Areas Commun.*, vol. 40, no. 6, pp. 1728–1767, 2022.
- [2] J. G. Andrews, S. Buzzi, W. Choi, S. V. Hanly, A. Lozano, A. C. Soong, and J. C. Zhang, "What will 5G be?" *IEEE J. Sel. Areas Commun.*, vol. 32, no. 6, pp. 1065–1082, 2014.
- [3] A. Conti, F. Morselli, Z. Liu, S. Bartoletti, S. Mazuelas, W. C. Lindsey, and M. Z. Win, "Location awareness in beyond 5G networks," *IEEE Commun. Mag.*, vol. 59, no. 11, pp. 22–27, 2021.
- [4] Z. Xiao and Y. Zeng, "An overview on integrated localization and communication towards 6G," *Sci. China Inf. Sci.*, vol. 65, no. 3, p. 131301, 2022.
- [5] W. Wang and W. Zhang, "Joint beam training and positioning for intelligent reflecting surfaces assisted millimeter wave communications," *IEEE Trans. Wireless Commun.*, vol. 20, no. 10, pp. 6282–6297, 2021.
- [6] J. Li, Y. Niu, H. Wu, B. Ai, S. Chen, Z. Feng, Z. Zhong, and N. Wang, "Mobility support for millimeter wave communications: Opportunities and challenges," *IEEE Commun. Surv. Tutor.*, vol. 24, no. 3, pp. 1816–1842, 2022.
- [7] M. Alsenwi, M. Abolhasan, and J. Lipman, "Intelligent and reliable millimeter wave communications for RIS-aided vehicular networks," *IEEE Trans. Intell. Transp. Syst.*, vol. 23, no. 11, pp. 21 582–21 592, 2022.
- [8] A. Ali, N. Gonzalez-Prelcic, R. W. Heath, and A. Ghosh, "Leveraging sensing at the infrastructure for mmwave communication," *IEEE Commun. Mag.*, vol. 58, no. 7, pp. 84–89, 2020.
- [9] A. Sesyuk, S. Ioannou, and M. Raspopoulos, "3D millimeter-wave indoor localization," in *2023 13th Int. Conf. Indoor Positioning Indoor Navig. (IPIN)*. IEEE, 2023, pp. 1–7.
- [10] M. Ruble and I. Güvenç, "Wireless localization for mmwave networks in urban environments," *EURASIP J. Adv. Signal Process.*, vol. 2018, pp. 1–19, 2018.
- [11] B. Zhou, A. Liu, and V. Lau, "Successive localization and beamforming in 5g mmwave MIMO communication systems," *IEEE Trans. Signal Process.*, vol. 67, no. 6, pp. 1620–1635, 2019.
- [12] Z. Aliyazicioglu, H. Hwang, M. Grice, and A. Yakovlev, "Sensitivity analysis for direction of arrival estimation using a Root-MUSIC algorithm," *Eng. Lett.*, vol. 16, no. 3, 2008.
- [13] P. Wang, J. Fang, X. Zeng, Z. Chen, and H. Li, "Low-complexity joint transceiver optimization for mmWave/THz MU-MIMO ISAC systems," *IEEE Internet Things J.*, 2024.
- [14] A. M. Elbir, K. V. Mishra, A. Abdallah, A. Celik, and A. M. Eltawil, "Spatial path index modulation in mmWave/THz band integrated sensing and communications," *IEEE Trans. Wireless Commun.*, 2024.
- [15] X. Cheng, D. Duan, S. Gao, and L. Yang, "Integrated sensing and communications (ISAC) for vehicular communication networks (VCN)," *IEEE Internet Things J.*, vol. 9, no. 23, pp. 23 441–23 451, 2022.
- [16] R. Zhang, Y. Zhang, R. Tang, H. Zhao, Q. Xiao, and C. Wang, "A joint UAV trajectory, user association, and beamforming design strategy for multi-UAV assisted ISAC systems," *IEEE Internet Things J.*, 2024.
- [17] Y.-N. R. Li, B. Gao, X. Zhang, and K. Huang, "Beam management in millimeter-wave communications for 5G and beyond," *IEEE Access*, vol. 8, pp. 13 282–13 293, 2020.
- [18] C. Qi, W. Ci, J. Zhang, and X. You, "Hybrid beamforming for millimeter wave mimo integrated sensing and communications," *IEEE Commun. Lett.*, vol. 26, no. 5, pp. 1136–1140, 2022.
- [19] M. Xiong, Q. Liu, S. Zhou, S. Han, and M. Liu, "Performance of a high power and capacity mobile SLIPT scheme," *IEEE Trans. Commun.*, vol. 70, no. 7, pp. 4717–4730, 2022.
- [20] M. Liu, Q. Jiang, M. Xu, and Q. Liu, "Passive location estimation via resonant beam," *IEEE Trans. Veh. Technol.*, vol. 72, no. 10, pp. 13 055–13 066, 2023.
- [21] W. Wang, Q. Zhang, H. Lin, M. Liu, X. Liang, and Q. Liu, "Wireless energy transmission channel modeling in resonant beam charging for IoT devices," *IEEE Internet Things J.*, vol. 6, no. 2, pp. 3976–3986, 2019.
- [22] H. Deng, S. Zhao, M. Liu, and Q. Liu, "Joint sensing and power transfer via distributed coupled-cavity lasers," *IEEE Internet Things J.*, 2023.
- [23] Y. Guo, Q. Jiang, M. Xu, W. Fang, Q. Liu, G. Yan, Q. Yang, and H. Lu, "Resonant beam enabled DoA estimation in passive positioning system," *IEEE Trans. Wireless Commun.*, vol. 23, no. 11, pp. 16 290–16 300, 2024.
- [24] Y. Guo, M. Xiong, W. Fang, Q. Jiang, M. Xu, Q. Liu, and G. Yan, "Resonant beam enabled passive 3D positioning," *IEEE Internet Things J.*, pp. 1–1, 2025.
- [25] Q. Jiang, M. Liu, M. Xu, W. Fang, M. Xiong, Q. Liu, and S. Zhou, "Single-frequency self-alignment RF resonant beam for information and power transfer," *IEEE Internet Things J.*, vol. 12, no. 11, pp. 16 622–16 636, 2025.
- [26] X. Song, X. Li, X. Qin, and J. Xu, "Fully-passive versus semi-passive IRS-enabled sensing: SNR analysis," in *2023 IEEE Globecom Workshops (GC Wkshps)*. IEEE, 2023, pp. 1874–1879.
- [27] A. Winterstein, L. A. Greda, and A. Dreher, "A PLL-based retro-directive antenna system for communications with arbitrary frequency gaps," in *2015 9th Eur. Conf. Antennas Propag. (EuCAP)*. IEEE, 2015, pp. 1–5.
- [28] V. Fusco, C. B. Soo, and N. Buchanan, "Analysis and characterization of PLL-based retrodirective array," *IEEE Trans. Microw. Theory Tech.*, vol. 53, no. 2, pp. 730–738, 2005.
- [29] N. B. Buchanan, V. F. Fusco, and M. van der Vorst, "SATCOM retrodirective array," *IEEE Trans. Microw. Theory Tech.*, vol. 64, no. 5, pp. 1614–1621, 2016.
- [30] N. Buchanan, V. Fusco, and M. Van Der Vorst, "A high performance analogue retrodirective phase conjugation circuit with RX array factor combination ability," in *2011 IEEE MTT-S Int. Microw. Symp.*. IEEE, 2011, pp. 1–4.
- [31] B. Friedlander, "Localization of signals in the near-field of an antenna array," *IEEE Trans. Signal Process.*, vol. 67, no. 15, pp. 3885–3893, 2019.
- [32] Y. Kang, X. Q. Lin, Y. Li, and B. Wang, "Dual-frequency retrodirective antenna array with wide dynamic range for wireless power transfer," *IEEE Antennas Wireless Propag. Lett.*, vol. 22, no. 2, pp. 427–431, 2022.
- [33] B. S. Guru and H. R. Hiziroglu, *Electromagnetic field theory fundamentals*. Cambridge Univ. Press, 2009.
- [34] H. Farès, B. Vrigneau, and O. Berder, "Green communication via harq protocols using message-passing decoder over AWGN channels," in *2015 IEEE Annu. Int. Symp. Pers. Indoor Mobile Radio Commun. (PIMRC)*. IEEE, 2015, pp. 197–201.
- [35] S. Kim, H.-W. Jo, J.-W. Kim, J.-I. Oh, J.-W. Yu, and B. Ahn, "Curved-retrodirective beamforming system to improve microwave power transmission efficiency in the Fresnel region," *IEEE Internet Things J.*, vol. 10, no. 17, pp. 15 012–15 024, 2023.
- [36] S. Dutta, C. N. Barati, D. Ramirez, A. Dhananjay, J. F. Buckwalter, and S. Rangan, "A case for digital beamforming at mmwave," *IEEE Trans. Wireless Commun.*, vol. 19, no. 2, pp. 756–770, 2019.
- [37] J.-Y. Lee, S.-H. Lee, H. Kim, and H.-K. Yu, "A 28.5–32-GHz fast settling multichannel PLL synthesizer for 60-GHz WPAN radio," *IEEE Trans. Microw. Theory Tech.*, vol. 56, no. 5, pp. 1234–1246, 2008.
- [38] C. A. Balanis, *Antenna theory: analysis and design*. John Wiley & Sons, 2016.
- [39] S. H. A. Shah, S. Aditya, and S. Rangan, "Power-efficient beam tracking during connected mode drx in mmwave and sub-thz systems," *IEEE J. Sel. Areas Commun.*, vol. 39, no. 6, pp. 1711–1724, 2021.
- [40] A. R. Carballeira, F. A. de Figueiredo, and J. M. C. Brito, "Simultaneous estimation of azimuth and elevation angles using a decision tree-based method," *Sensors*, vol. 23, no. 16, p. 7114, 2023.